RSC Advances

PAPER

View Article Online
View Journal | View Issue

Cite this: *RSC Adv.*, 2026, **16**, 1900

Ultra-high surface area silica material and its application for selective *N*-formylation using a CO_2 surrogate

Muhammad Anwar, *[a] Soyeb Pathan, †[a] Pogula Sreekanth Reddy,[a] Janarthanan Ponraj[b] and Sarim Dastgir ‡*[a]

Received 28th September 2025
Accepted 18th December 2025

DOI: 10.1039/d5ra07379k

rsc.li/rsc-advances

A sustainable room temperature synthesis of ultra-high surface area mesoporous silica material (1653 $m^2 g^{-1}$), designated as QSM-2, has been developed using tetraethyl orthosilicate, cetyltrimethylammonium bromide (CTAB), and β-cyclodextrin (β-CD) as the silicon source, structure directing agent, and additive, respectively. The process was optimised by varying key reaction parameters, including the amount of additive, reaction temperature and sonication, while maintaining a constant silica-to-surfactant ratio. Scale-up studies confirmed reproducibility at a 20-gram scale, highlighting the method's potential for large scale applications. The material with an ultra-high surface area was evaluated for the *N*-formylation of amines using formic acid as a benign C_1 source, thereby enabling the indirect utilisation of CO_2. This work presents a sustainable and selective protocol for converting a wide range of amines to the corresponding formamides under mild, solvent-free conditions, achieving excellent yields (up to 99%), and high selectivity (100%).

Introduction

Since the discovery of periodic mesoporous silicas (M41S) using long-chain surfactant molecules as structure-directing agents by the Mobil Oil Company,[1,2] the development of a wide range of novel materials has accelerated over their zeolitic counterparts. This is attributed to their large surface area, mesoporosity, tuneable pore size and structure, controllable morphology, and ease of surface functionalisation. This supramolecular guided approach has led to a family of porous materials such as MCM,[3,4] SBA,[5] FSU,[6,7] KIT[8] and MSU,[9] whose physical and morphological properties can be tuned during synthesis by varying reaction parameters, stoichiometry of substrates, the nature of surfactant molecule, and additives, or *via* post-synthesis functionalisation techniques.

The remarkable features of mesoporous silicas, including high specific surface area, tuneable pore size, large pore volume, and facile surface functionalisation, make them promising candidates for diverse applications such as drug delivery systems, sensors, optical devices and imaging, energy, catalysis, and adsorption.[10–17] These applications are feasible due to their exceptionally high surface areas with uniform pore sizes, high thermal stability, and excellent adsorption capacity. Among the M41S family, MCM-41 with hexagonal pores in a honeycomb arrangement and MCM-48 with cubic symmetry are the most significant for practical applications across various fields, whereas the mesoporous structure of lamellar MCM-50 collapses upon calcination, limiting its utility.[18–20]

Particularly, MCM-48, which possesses a cubic phase with *Ia3d* symmetry, consists of interwoven three-dimensional channels and a gyroid-like structure, with mesopores separated by thin walls of amorphous silica. This unique physical morphology makes MCM-48 an ideal candidate for applications in catalysis and separation technologies, as its 3D channel network offers superior mass transfer kinetics compared to the unidirectional pore system of MCM-41.[21–23] Typically, mesoporous MCM-48 is synthesised *via* hydrothermal methods in a strong basic medium. However, challenges in achieving reproducibility in physical properties, purity, and yield have limited process optimisation, including investigations into the effects of co-templates as well as additives on MCM-48 morphology, leaving this area relatively undeveloped.

In 1999, Schumacher *et al.*[24] modified traditional hydrothermal conditions and reported a fast and convenient method for synthesising spherical MCM-48 particles in the micrometre and submicrometre size with very high surface area. Since then, to achieve the desired physical properties and morphologies while enhancing process sustainability,[25] researchers have studied the effects of various parameters, including mixed

[a]*Qatar Environment and Energy Research Institute (QEERI), Hamad Bin Khalifa University, Qatar Foundation, PO Box 34110, Doha, Qatar. E-mail: muanwar@hbku.edu.qa; sarim.dastgir@lmh.oxon.org*

[b]*Materials Core Laboratories, Hamad Bin Khalifa University, Qatar Foundation, PO Box 34110, Doha, Qatar*

† Current address: Department of Chemistry, Parul Institute of Applied Sciences, Parul University, Vadodara, Gujarat 391760, India.

‡ Current address: Green Global Group (G3) of Companies, 3183 Wilshire Boulevard, Los Angeles, CA, 90010, USA.

Table 1 Modified processes for improvement of physical properties of MCM-48 type and analogue silica

S. no	Surfactant/additive	Reaction conditions (time, temp/calcination temperature)	Material properties (BET surface area, pore volume, pore size)
1	Mixed surfactant (CTAB/SDS)[25]	72 h, 100 °C/600 °C for 6 h	861.8 $m^2 g^{-1}$, 0.862 $cm^3 g^{-1}$, 27.2 Å
2	Mixed surfactant (pluronic P123/CTAB)[26]	48 h, 100 °C/550 °C for 5 h	1500 $m^2 g^{-1}$, 1.5 $cm^3 g^{-1}$, 40 Å Note: exceptional hydrothermal stability
3	Mixed surfactant (PVP/CTAB)[28]	3 days, 100 °C/550 °C for 6 h	1870 $m^2 g^{-1}$, NR, 23.2 Å Note: silanol-Rich MCM-48
4	Mixed templates (o-C_nPOC$_m$/CTAB)[29]	4 h, RT, 900 °C for 5 h	980 $m^2 g^{-1}$, 0.44 $cm^3 g^{-1}$, <20 Å Note: unusually high thermal stability
5	Triton X-100 (ref. 31)	4 days, 100 °C, 600 °C	1150 $m^2 g^{-1}$, 1.25 $cm^3 g^{-1}$, 40.1 Å Note: broad distribution of average pore sizes;
6	Gemini surfactant[27,32]	2 days, 100 °C, 550 °C for 5 h	1164 $m^2 g^{-1}$, 0.58 $cm^3 g^{-1}$, 25 Å Note: narrow pore size distribution
7	Pluronic F127 (ref. 33)	150 °C, 600 °C	1248 $m^2 g^{-1}$, 0.96 $cm^3 g^{-1}$, 23–33 Å Note: monodisperse spherical MCM-48
8	CTAB with fluoride ion induced synthesis[39]	72 h, 100 °C	1281 $m^2 g^{-1}$, NR, 24 Å Note: reduction of CTAB template amount
9	Citric acid (CA) as additive[41]	6 days, 50 °C/500 °C for 2 h	1015 $m^2 g^{-1}$, 1.48 $cm^3 g^{-1}$, 58 Å
10	CTAB with fluoride as counterion[42]	2 days, 30–50 °C/550 °C for 6 h	1262 $m^2 g^{-1}$, 1.08 $cm^3 g^{-1}$, 63.0 Å Note: Ordered earthworm-like mesoporous silica
11	CTAB[43]	16 h, RT/540 °C for 9 h	1855 $m^2 g^{-1}$, 0.824 $cm^3 g^{-1}$, 21.8 Å
12	Gemini surfactant[44]	2 days, 100 °C/550 °C	1600 $m^2 g^{-1}$, 1.4 $cm^3 g^{-1}$, 13.1 Å Note: Improved material quality
13	CTAB[45]	2–24 h, RT/600 °C for 6 h	1010 $m^2 g^{-1}$, 0.8 $cm^3 g^{-1}$, 33 Å Note: Highly ordered uniform spheres of size
14	CTAB with β-cyclodextrin (current Work)	2 h, RT/550 °C for 5 h	1653 $m^2 g^{-1}$, 1.08 $cm^3 g^{-1}$, 2.64 Å Note: High surface area with uniform particle size distribution

surfactants,[26–32] organic–inorganic additives,[33–40] and other synthesis variables, to tailor the properties of MCM-48 under both hydrothermal and non-hydrothermal conditions. These modified protocols, summarised in Table 1, demonstrate improvements in key physical properties such as pore size, pore volume, monodispersity of spheres, thermal stability, surface silanol groups, and surface area.

The encouraging results reported in the literature, especially the enhancement of specific surface area along with spherical morphology,[26,28,29,31–33,39,41–45] motivated us to explore the effect of a dextrin-based additive under room temperature conditions and short reaction times. Accordingly, in the present study, β-cyclodextrin was selected as an additive to modify the conventional sol–gel synthesis of mesoporous silica.

β-Cyclodextrin, a cyclic oligosaccharide biopolymer with toroidal shape, features a hydrophilic exterior and lipophilic internal cavities, conferring a strong affinity to form host-guest inclusion with broad range of organic and inorganic molecules.[46,47] It is believed to form supramolecular assemblies with quaternary alkylammonium surfactants such as cetyltrimethylammonium bromide (CTAB), thereby changing the morphology of the resulting material. The addition of β-cyclodextrin, prior to silica condensation, facilitates the development of pores within the silica particles.[48,49] Given these advantageous properties, we investigated the effect of β-cyclodextrin as an additive in the sol–gel synthesis of mesoporous ordered silica materials at room temperature. In this manuscript, the beneficial role of β-cyclodextrin in combination with CTAB was explored as a templating agent responsible for pore formation, pore size and as a structure directing agent for a room temperature synthesis of high surface area materials. In addition, the effects of sonication and temperature on the physical properties of the synthesised silica (abbreviated as QSM), such as surface area, morphology, and particle size distribution, were investigated. The materials were characterised and preliminarily screened using scanning electron microscopy (SEM), BET surface area analysis, and transmission electron microscopy (TEM). Scalability and repeatability studies were conducted, and a successful scale-up procedure was established at 20 g scale. Further characterisation of the synthesised silica was carried out using low-angle powder X-ray diffraction (PXRD), small-angle X-ray scattering (SAXS), focused ion beam-transmission electron microscopy (FIB-TEM), Fourier-transform infrared spectroscopy (FT-IR), and solid state ^{29}Si cross-polarisation magic angle spinning (CP/MAS) NMR spectroscopy. The ultra-high surface area silica material was subsequently investigated for catalytic applications for amide bond formation, highlighting its potential as a sustainable catalyst in solvent-free and energy-efficient synthetic processes.[50]

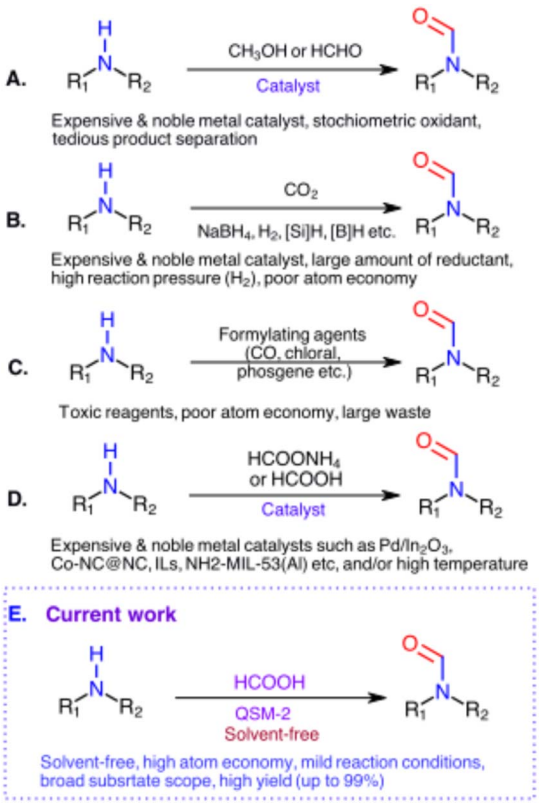

Scheme 1 Synthetic methodologies for *N*-formylation of amines.

The *N*-formylation of amines is adopted as a benchmark reaction for evaluating the initial catalytic performance of QSM silica materials, as it represents one of the most effective, facile, and chemoselective strategies for the synthesis of formamides.[51] Formamides are versatile building blocks extensively utilised in the synthesis of bioactive molecules, heterocycles, agrochemicals, and pharmaceuticals, owing to the broad utility of *N*-formylated derivatives as protecting groups and precursors for complex heterocyclic frameworks.[52–56] Few notable examples of formamide containing drugs include benfotiamine (for diabetic neuropathy),[57] formoterol (for lung disease treatment),[58] fursultiamine (for thiamine deficiency),[59] and vincristine (an anticancer agent).[60] Formamides also play an important role as protecting groups of amines in peptide synthesis.[61] Moreover, they function as useful reagents in biochemistry and molecular biology, particularly in nucleic acid research.[62–64] Because of their broad applications, various methodologies have been developed for formamide synthesis using formylating agents such as chloral,[65] ammonium formate,[66,67] acetic formic anhydride,[68] ethyl formate,[69] *N*,*N*-dimethylformamide,[70] formyloxyacetoxyphenylmethane,[71] methanol,[72,73] carbon dioxide,[64,74] and formic acid (HCOOH).[62,75] Comparatively, the reductive functionalisation of CO_2 offers an environmentally benign synthetic route to formamides.[76]

However, this often involves expensive or noble metal complexes and reducing agents such as boranes,[77] hydrogen[64,74,78–81] or hydrosilanes.[82–84] Despite their advantages, many of these methodologies have limitations, including harsh reaction conditions, high temperature and pressure, long reaction times, low yields, substantial by-product formation, and poor atom economy (Scheme 1).[85–90] Therefore, the development of new methodologies remains highly desirable and presents a great challenge in advancing sustainable synthesis.

In recent years, formic acid has increasingly been recognised as an effective formylating agent due to its low cost, low toxicity, and easy accessibility from biomass-derived renewable sources.[74,91,92] Traditional *N*-formylation methodologies typically rely on harsh reagents or transition metal catalysed homogeneous catalytic systems, which often generate significant chemical waste and introduce complexities in downstream purification. These limitations underscore the need for more sustainable and operationally simple alternatives. Formic acid (HCOOH) offers a sustainable alternative and is regarded as an indirect carbon dioxide (CO_2) carrier. It can be synthesised through the catalytic hydrogenation of CO_2 using molecular hydrogen (H_2) in the presence of homogeneous or heterogeneous catalysts, such as ruthenium, iridium, or iron complexes and thus functions as a practical CO_2 surrogate for CO_2-derived C_1 synthon, aligning with principles of green chemistry and circular carbon economy.[93,94] Various studies have reported the *N*-formylation of primary and secondary amines with formic acid using noble metal catalysts such as gold (Au),[95] palladium (Pd),[96,97] platinum (Pt),[98] rhodium (Rh),[99] *etc.* Recently, a $Mo^{VI}O_6$ supported iron(III) catalyst was employed for coupling of formic acid with amines to synthesise formamides.[75] In addition, Liang *et al.* reported the *N*-formylation of amines using formic acid under catalyst-free conditions.[100] However, this required temperatures of 150 °C and prolonged reaction times.

In the context of green and sustainable chemistry, there remains a pressing need for the development of efficient and environmentally benign methodologies under mild reaction conditions with enhanced atom economy and reduced energy consumption. Given these considerations, the development of mild, solvent and metal free heterogeneous catalytic protocols for *N*-formylation is highly desirable. Such approaches promise to minimise environmental impact, simplify reaction handling, and enhance the overall sustainability of the process. Consequently, we explored the *N*-formylation of amines using formic acid as a carbonyl source in the presence of a catalytic amount of QSM materials. Upon optimisation of reaction conditions, QSM materials were found to be highly effective for the *N*-formylation of both primary and secondary amines, yielding the corresponding formamides in excellent yields and with high selectivity.

Experimental

Materials

All chemicals were of analytical reagent grade and used without further purification. Tetraethyl orthosilicate (TEOS), β-cyclodextrin (β-CD), cetyltrimethylammonium bromide (CTAB), aqueous NH_3 (28% v/v), absolute ethanol, organic amines, formic acid, ethyl acetate, and hexane were purchased from Sigma-Aldrich and Fisher Scientific. Alumina-baked thin-layer chromatography (TLC) plates containing F_{254} UV indicator were

purchased from SiliCycle. RediSep® silica disposable flash columns were purchased from Teledyne Isco. All glassware was quantitatively cleaned using the standardised methodologies and then dried overnight at 130 °C before use.

Synthetic protocol for QSM materials

High surface area silica was synthesised using a modified method incorporating β-cyclodextrin as an additive.[45] In a typical procedure, β-cyclodextrin and cetyltrimethylammonium bromide were dissolved in 100 mL of 1 : 1 (v/v) mixture of deionised water and ethanol. The mixture was stirred at 300 rpm, and 15 mL of aqueous ammonia solution (28–30%) was added dropwise. After 60 minutes, tetraethylorthosilicate was added dropwise. The resulting solution was aged at room temperature with continuous stirring at 400 rpm for 2 hours. The product was isolated by centrifugation at 10 000 rpm for 10 minutes, washed three times with water (25 mL) and ethanol (25 mL), air dried, and calcined in a furnace at 550 °C for 6 hours to obtain mesoporous silica nanoparticles.

Procedure for *N*-formylation of amines

A mixture of amine (1.0 mmol), formic acid (5.0 mmol), and silica (2.0 mg) was stirred in a 10 mL glass vial at 70 °C or 100 °C for 1–1.5 hours. The reaction was monitored by TLC using 1 : 3 mixture of ethyl acetate to hexane as mobile phase. Upon completion, the mixture was diluted with ethyl acetate (10 mL) and filtered to remove the silica. The filtrate was extracted with ethyl acetate (2 × 10 mL). The organic layer was washed with brine and dried over anhydrous Na_2SO_4. The solvent was removed *in vacuo*, and the crude product was purified by flash column chromatography to obtain the pure formamide.

Material characterisation

FT-IR spectra were recorded in the wavenumber range of 4000–400 cm^{-1} using a PerkinElmer spectrometer, with samples prepared as discs by pressing with dried KBr. Brunauer–Emmett–Teller (BET) surface area measurements were performed using a Micromeritics ASAP 2420 volumetric static adsorption instrument with nitrogen adsorption at 77 K. Pore size distributions were calculated using the Barrett–Joyner–Halenda (BJH) adsorption–desorption isotherms. Scanning electron microscopy images were recorded using a Quanta 650 Schottky Field Emission Scanning Electron Microscope. Transmission electron microscopy bright-field imaging was carried out using a Thermo Scientific Talos F200X operated at 200 kV. Silica powder was dispersed in isopropyl alcohol, sonicated (~5 min), and drop-cast onto 300-mesh Cu lacey carbon grids. Samples were air-dried and imaged under low-dose conditions to minimise beam damage. FIB-TEM lamellae were prepared using an FEI Versa 3D DualBeam system equipped with a Ga^+ ion source. The sample was first coated with a protective Pt layer *via* gas injection, followed by trench milling and lift-out using an Easylift micromanipulator. The lamellae were then mounted onto TEM grids for imaging and analysis. Final thinning to electron transparency (~50 nm) was performed at low ion beam currents to minimise damage. Low-angle powder XRD analysis was performed using a Rigaku Smart Lab X-ray diffractometer with Cu-Kα radiation ($\lambda = 1.5418$ Å), operating at 40 kV and 30 mA, with 2θ range of 1° to 7° and step size of 0.02°. Small-angle X-ray scattering analysis was carried out using a Rigaku S-MAX 3000 system equipped with a MicroMax tube source operating at 45 kV and 0.66 mA. Distance and beam-centre calibration was performed using silver behenate. All analyses were performed under vacuum and at room temperature.

Solid State ^{29}Si CP/MAS NMR measurements were performed using a Bruker Avance III WB 600 MHz DNP NMR spectrometer operating at 14.1 T, employing a 3.2 mm Triple Resonance HXY probe. Samples were packed into 3.22 mm zirconia rotors and spun at a magic-angle spinning rate of 10 kHz. The ^{29}Si chemical shifts were referenced to tetramethylsilane (TMS), as an external standard. Solution NMR spectra were recorded on Bruker Avance Neo NB 400 MHz and Avance III HD SB 800 MHz NMR spectrometers. Chemical shifts (δ) are reported in ppm downfield from tetramethylsilane. The degree of condensation (DC) for silica material was computed using ^{29}Si NMR signals for Q^2, Q^3 and Q^4 silicon sites.[101]

$$\mathrm{DC}(\%) = \frac{\sum_n nq^n}{f}$$

where, "n" is defined as the degree of substitution or number of condensed functional groups, *i.e.*, Si–O–Si bonds for a silicon atom. "q^n" refers to the molar fraction or relative population of species with "n" condensed bonds. This is derived from the integration (peak areas/intensities) of the corresponding signals in ^{29}Si NMR spectrum. The "f" denotes the maximum possible functionality (valency) of the monomer unit. DC value represents the extent to which available reactive sites on monomer units have formed covalent bonds (condensed) into a larger silica network. A value of 100% indicates a fully condensed, cross-linked structure. For Q species (silica network units *i.e.*, SiO_2), the maximum functionality is $f = 4$. For Q^n species, the corresponding Q^2, Q^3 and Q^4 signals appear in distinct chemical shift ranges. In ^{29}Si NMR spectrum, the more shielded silicon atom $Si(OSi)_2(OH)_2$ (Q^2) appears downfield of the less shielded silicon atom $Si(OSi)_4$ (Q^4). Q^2 and Q^3 values were further used to calculate the silanol density (ρ) in OH/nm^2 using the formula.[102,103]

$$\rho = \frac{\left(\left(X_{Q^2} \times 2\right) + \left(X_{Q^3} \times 1\right)\right) \times N_A}{M_{SiO_2} \times \mathrm{SSA}}$$

where: X_{Q^2} & X_{Q^3} are the molar fraction of Q^2 and Q^3 sites N_A is Avogadro's Constant (6.022×10^{23} mol^{-1}) M_{SiO_2} is the molar mass of SiO_2 (60.08 g mol^{-1}) SSA is determined by BET analysis (m^2 g^{-1}).

Result and discussion

β-Cyclodextrin, a cyclic oligosaccharide, naturally self-assembles into aggregates in aqueous solutions. When added before the silica condensation step, these aggregates act as pore-forming agents within the silica matrix. The present synthetic procedure employs β-cyclodextrin as an additive to

Table 2 Surface area optimisation studies for QSM materials

S. no.	Chemical composition: TEOS (g)	CTAB (g)	β-CD (g)	1 : 1 ethanol/ H_2O (mL)	NH_3 (mL)	Aging condition	S.A ($m^2\ g^{-1}$)	PV ($cm^3\ g^{-1}$)	PD (nm)	Comment/observation from SEM	Material designation
a	3.45	2.4	0.3	100	15	RT/stirring	1572	1.01	2.50	Defected spheres, broad particle size distribution	QSM-1
b	3.45	2.4	0.65	100	15	RT/stirring	1653	1.08	2.64	Optimised condition: high surface area with better particle size distribution	QSM-2
c	3.45	2.4	0.9	100	15	RT/stirring	1574	0.99	2.70	Broad particle size distribution, higher amount of additive	QSM-3
d	3.45	2.4	0.65	100	15	RT/sonication	1293	0.9	2.48	Defected spheres, broad particle size distribution, relatively low surface area	QSM-4
e	3.45	2.4	0.65	100	15	0 °C/stirring	1186	0.83	2.50	Broad particle size distribution, relatively low surface area	QSM-5
f	3.45	2.4	0.65	100	15	50 °C/stirring	1295	0.97	2.46	Broad particle size distribution, relatively low surface area	QSM-6

produce mesoporous silica materials with ultra-high surface area. Initially, the aim was to synthesise β-CD-functionalised silica in a single step. However, repeated attempts revealed that β-CD was either partially or completely degraded, or detached during the template removal process, whether *via* thermal treatment or Soxhlet extraction. Despite this setback, the inclusion of β-CD significantly influenced the surface area and morphology of the final material after air calcination. Consequently, the research focus shifted toward optimising the synthesis and processing conditions to achieve the desired material properties. This optimisation involved systematic variation of synthesis parameters for QSM-2 material, and the resulting silica was characterised using scanning electron microscopy and BET surface area analysis. A summary of the data, correlated with reaction parameters, is presented in Table 2.

The effect of the additive on physical properties and morphology of silica was investigated using different amounts of β-CD. SEM images indicate that increasing the additive from 0.3 g (Fig. 1a) to 0.65 g (Fig. 1b), and further to 0.9 g (Fig. 1c), resulted in materials with comparable surface areas typically exceeding 1500 $m^2\ g^{-1}$. The typical size of the synthesised silica spheres obtained with 0.65 g β-CD was in the range of 500 ± 100 nm. However, a broad particle size distribution was observed for 0.9 g β-CD (Table 2, entry c), ranging from 300 nm to several microns. Moreover, higher additive concentrations

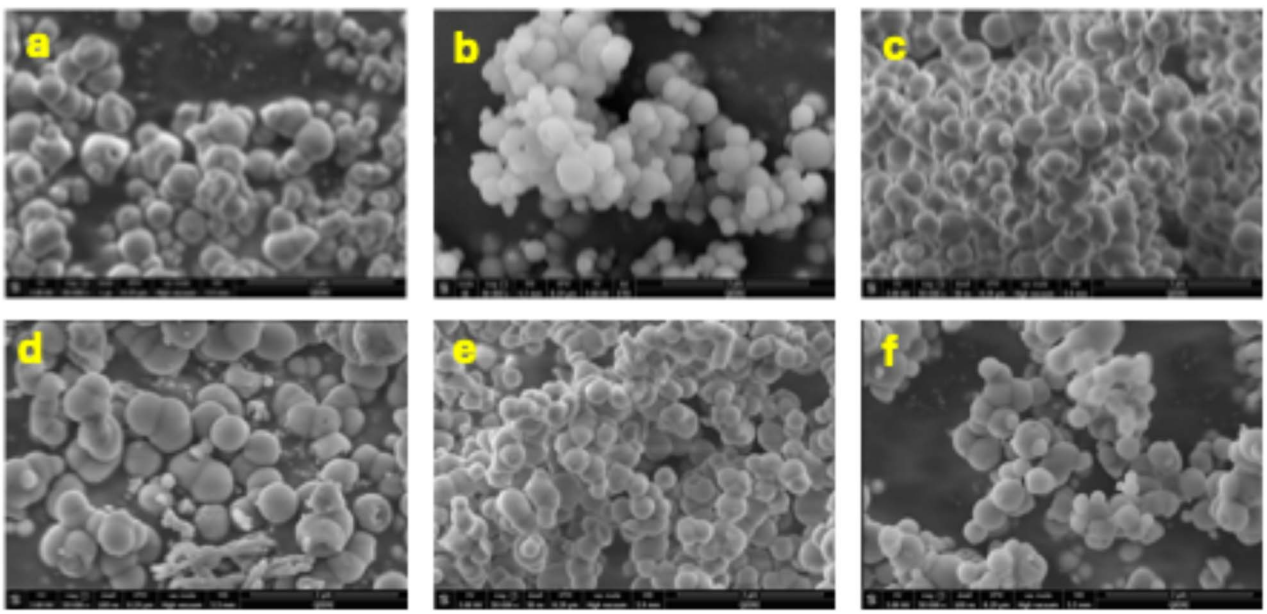

Fig. 1 SEM images for silica synthesised using β-CD amount; (a) 0.3 g, (b) 0.65 g, (c) 0.9 g, (d) sonication, (e) 0 °C, (f) 50 °C

led to a transformation from defective spheres to nearly spherical morphology with minimal defects. Therefore, β-CD has contributed to the overall control of shape and pore volume. The interaction of β-CD with CTAB is considered to be physical rather than a chemical complexation in enhancing morphology and surface area for QSM materials.[48,49] Although no significant morphological differences were observed between silica samples synthesised with 0.65 g and 0.9 g of additive, the former provided the highest surface area with a more uniform particle distribution. Therefore, 0.65 g of β-CD was selected as the optimised amount for further studies. To investigate the effect of reaction conditions, synthesis was carried out under sonication, and the resulting material was characterised by SEM. A comparison of SEM images of silica materials synthesised by stirring (Fig. 1b) and sonication (Fig. 1d) reveals that the former yields predominantly spherical particles. In contrast, silica obtained under sonication exhibited spheres with non-uniform diameters, structural lacunae, and regions of non-structural bulk silica. This result may be attributed to non-uniform sonication and the associated temperature increase during synthesis. Moreover, the presence of bulk silica under sonication conditions led to a significant decrease in surface area. High surface area silica was also synthesised at different temperatures, and the surface morphologies of the resultant materials are presented in Fig. (1b, e and f). The increase in temperature from room temperature (RT) to 50 °C significantly affected the particle size distribution, resulting in uneven spheres (Fig. 1f), likely due to further condensation of Si–OH groups at elevated temperatures. Conversely, a decrease in temperature to 0 °C (Fig. 1e) resulted in silica with uniform spheres. This observation may be attributed to controlled hydrolysis of TEOS as well as condensation. However, this was accompanied by a reduction in particle size and surface area. Based on SEM observations and surface area results, the reaction conditions were optimised for further studies. The following are the optimised conditions:

- Composition: TEOS: 3.45 g, CTAB: 2.4 g, β-CD: 0.65 g 1 : 1 ethanol/H_2O (mL): 100 mL, 28–30% $NH_{3(aq)}$: 15 mL.
- Time and temperature: 2 h with stirring at room temperature.
- Calcination: 550 °C for 6 h.

The N_2-physisorption isotherms of silica synthesised under optimised conditions (denoted as QSM-2), and the scaled-up silica (denoted as QSM-2-SU) displayed sharp steps in the P/P_o range of 0.1–0.3 (Fig. 2), which were attributed to capillary condensation within the channels of these materials. The sharpness of these steps also confirmed the presence of a narrow pore size distribution and uniform pore channels.[45]

In addition, both isotherms exhibited reversible Type IV nature with H4 hysteresis, which was a characteristic of mesoporous family.[104] A very low gap between the adsorption and desorption isotherms suggested the presence of narrow cylindrical mesopores. N_2-physisorption studies showed that synthesised silica has surface area of 1653 $m^2\ g^{-1}$, a pore volume of 1.05 $cm^3\ g^{-1}$, and a pore diameter of 2.5–2.6 nm (Fig. 2). The physical properties of the scaled-up silica, QSM-2-SU (Fig. 2), were found to be comparable, with a surface area of 1680 $m^2\ g^{-1}$, a pore volume of 1.07 $cm^3\ g^{-1}$, and a very narrow pore size distribution with an average pore diameter of 2.6 nm.

There were no significant changes in shape and morphology after scale-up, as evident from SEM and TEM images (Fig. 3).

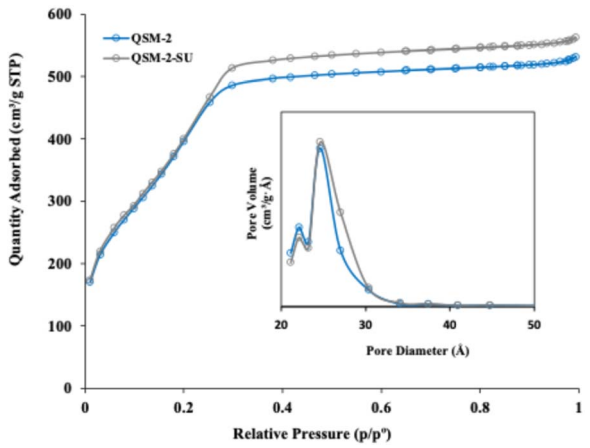

Fig. 2 N_2-physisorption analysis data for QSM-2 and QSM-2-SU.

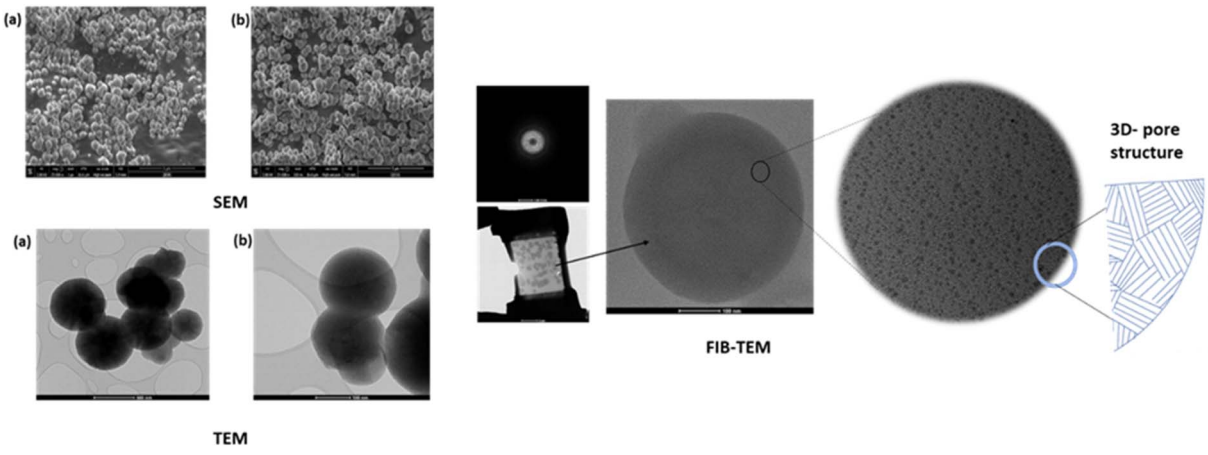

Fig. 3 SEM and TEM of silica. (a) QSM-2; (b) QSM-2-SU; FIB-TEM images for QSM-2-SU.

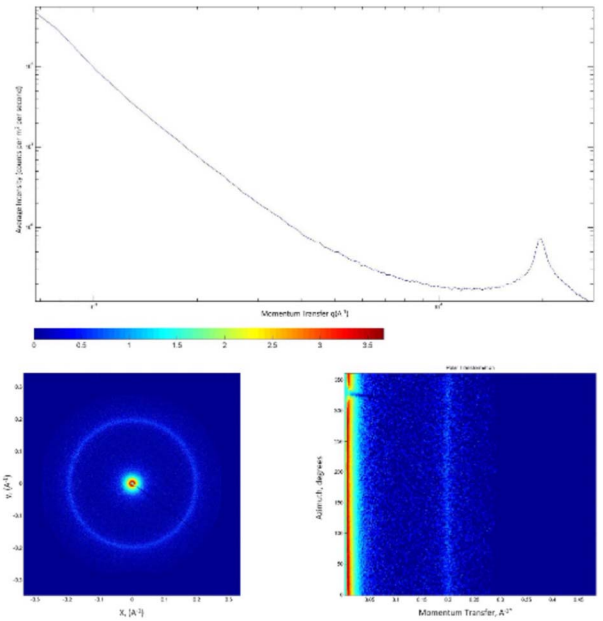

Fig. 4 SAXS (*I vs. q* 1D-plot) of QSM-2-SU silica.

However, due to the relatively large size of the spheres (about 500 nm), TEM alone was found inadequate to provide information regarding the type of porosity and core structure of the spheres. Therefore, the sample was prepared precisely by Focused Ion Beam (FIB) milling to create specific cross sections, followed by TEM analysis for detailed investigation. FIB-TEM (Fig. 3) images clearly revealed the presence of zigzag or 3D channels in all directions throughout the silica matrix, confirming that the silica spheres are highly porous and structurally analogous to MCM-48. To further confirm the FIB-TEM and N_2-physisorption results, small-angle X-ray scattering (SAXS) and low-angle powder X-ray diffraction (PXRD) analyses were performed. The SAXS pattern and 1D plot (Fig. 4), as well as the low angle XRD (Fig. 5), showed a single diffraction peak corresponding to the (211) plane at $2\theta = 2.67°$, with *d*-spacing of 31.87 Å (from XRD) and 32.03 Å (from SAXS), indicative of cubic symmetry (*Ia*3*d*). In addition to the main peak at around 3.1° 2θ, the additional peaks of lower intensity in the region 4–6° 2θ could be attributed to the (220), (400) and (321) planes,

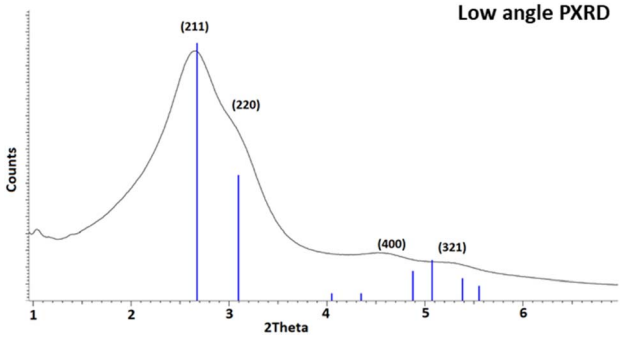

Fig. 5 Low angle powder XRD of QSM-2-SU material.

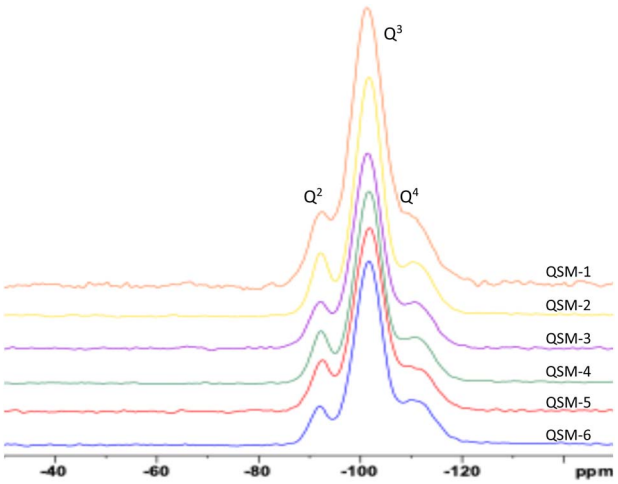

Fig. 6 ^{29}Si CP/MAS NMR spectra of QSM materials.

respectively.[105] The cell parameter (a) and wall thickness, calculated from SAXS and BET data, were found to be 78.4 Å and 12.4 Å, respectively.

Thus, the results obtained from all characterisation techniques confirmed that the synthesised silica possesses a very high surface area with short-range channels in all directions or a zigzag pattern, confirming the high purity mesoporous silica. Moreover, the FT-IR spectrum of scale-up MCM-48 type silica (Fig. S5) shows the characteristic bands of Si–O (δ, 463 cm^{-1}), Si–OH (957 cm^{-1}, ν_s), Si–O–Si (1118 cm^{-1}, ν_s; 802 cm^{-1}, ν_{as}), OH (3433 cm^{-1}), and H_2O (1635 cm^{-1}).

The ^{29}Si CP/MAS NMR spectra for QSM materials, shown in Fig. 6, exhibit resonances at −91.8 ppm, −100.9 ppm, and −109.9 ppm, corresponding to Q^2, Q^3, and Q^4 sites, respectively. These signals arise from $Si(OSi)_2(OH)_2$, $Si(OSi)_3(OH)$, and $Si(OSi)_4$, respectively. The relatively narrow line widths indicate well-ordered local ^{29}Si environments, reflecting a narrow distribution of chemical species, bond lengths, and bond angles.

The ^{29}Si NMR spectra (Fig. 6) were deconvoluted using Gaussian/Lorentzian line-shapes to identify individual peaks and determine the relative concentrations of Q^2, Q^3 and Q^4 type silicon sites. The degree of condensation (% DC) of silicon species was calculated using the previously described equation in the material characterisation section.[101] This metric represents the ratio of bridging oxygen atoms to the total number of

Table 3 Degree of condensation (% DC) and silanol density (ρ_{SiOH}) for QSM material

S. no.	Q^2 (%)	Q^3 (%)	Q^4 (%)	ρ_{SiOH} (nm^{-2})	% Geminals $Q^2/(Q^2+Q^3)$	% DC
QSM-1	19.3	58.7	22	6.2	24.7	75.7
QSM-2	15.2	58.4	26.4	5.4	20.7	77.8
QSM-3	16.1	60.1	23.8	5.9	21.1	76.9
QSM-4	14.1	61.4	24.5	6.9	18.7	77.6
QSM-5	17.1	60.5	22.4	7.9	22.0	76.3
QSM-6	12.7	61.8	25.5	6.7	17.0	78.2

Table 4 Optimisation of reaction conditions for catalytic *N*-formylation using QSM materials[a]

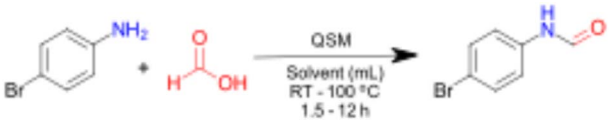

S. no.	Catalyst (mg)	HCOOH	Solvent	Temp (°C)	Time (h)	Yield (%)[b]
1	QSM-1 (10)	2 mL	CH_3CN	RT	12	76
2	QSM-2 (10)	2 mL	CH_3CN	RT	12	86
3	QSM-3 (10)	2 mL	CH_3CN	RT	12	69
4	QSM-4 (10)	2 mL	CH_3CN	RT	12	58
5	QSM-5 (10)	2 mL	CH_3CN	RT	12	59
6	QSM-6 (10)	2 mL	CH_3CN	RT	12	61
7	QSM-2 (10)	2 mL	CH_3CN	100	4	88
8	QSM-2 (10)	2 mL	Toluene	100	2	92
9	QSM-2 (10)	2 mL	DMF	100	2	90
10	QSM-2 (10)	2 mL	THF	100	2	85
11	QSM-2 (10)	2 mL	CH_3OH	100	2	78
12	QSM-2 (10)	2 mL	H_2O	100	2	64
13	QSM-2 (10)	2 mL	—	100	2	98
14	QSM-2 (5)	2 mL	—	100	2	98
15	QSM-2 (2)	2 mL	—	100	2	72
16	QSM-2 (0)	2 mL	—	100	2	41
17	QSM-2 (2)	4 mmol	—	100	2	68
18	QSM-2 (2)	5 mmol	—	100	1.5	98
19	QSM-2 (2)	5 mmol	—	70	6	89
20	QSM-2 (2)	5 mmol	—	RT	8	72

[a] Reaction conditions: 4-bromoaniline (1.0 mmol), RT = room temp. [b] Isolated yield.

oxygen atoms within the silicate network, providing a quantitative measure of structural connectivity of silicon atoms. A higher degree of condensation indicates a more polymerised network, which is often associated with enhanced thermal stability and reduced solubility. The concentration of silanol groups (ρ_{SiOH}) and the proportion of geminal silanols are in the range of 5.2–7.9 & 17.0–24.7% respectively (Table 3).

Our initial studies were focused on 4-bromoaniline as a model substrate for optimisation of catalytic *N*-formylation reaction using formic acid and mesoporous silica QSM materials (Table 4). When 4-bromo aniline (1.0 mmol) was reacted with formic acid (2.0 mL) in the presence of QSM materials (entry 1–6) in acetonitrile (CH_3CN) at room temperature, *N*-(4-bromophenyl) formamide was obtained in 86% yield after 12 h (Table 4, entry 2) with 100% selectivity for mono-formylation using QSM-2 as the most active catalyst material. Increasing the reaction temperature to 100 °C in acetonitrile reduced the reaction time to 4 h and slightly improved the yield to 88% (Table 4, entry 7). Subsequently, the effect of various other solvents, including DMF, toluene, THF, CH_3OH, and H_2O, was evaluated at 100 °C, all of which afforded the desired product in moderate to good yields (Table 4, entries 8–12). The highest isolated yield of 92% was obtained using toluene as a non-polar, aromatic organic solvent (Table 4, entry 8).

Notably, under solvent free conditions, the formamide product was obtained in 98% yield in 2 hours (Table 4, entry 13). To optimise the catalyst loading, the reaction was performed with reduced amounts of QSM-2 (Table 4, entries 13–15). Reducing the silica amount from 10 mg to 5 mg didn't affect the yield, which remained at 98% (Table 4, entry 14). However, a further reduction to 2 mg resulted in a significant drop in yield to 72% (Table 4, entry 15). In the absence of QSM-2, the reaction proceeded with only 41% yield under identical conditions (Table 4, entry 16), highlighting the crucial role of QSM-2 silica in catalysing the transformation. Further optimisation of the formic acid quantity was carried out using 4 mmol and 5 mmol in presence of 2 mg of QSM-2. The yield of the desired formamide was 68% with 4 mmol of formic acid, increasing to 98% with 5 mmol (Table 4, entries 17–18). Under optimised conditions (2 mg QSM-2 and 5 mmol HCOOH), the *N*-formylation reaction was also investigated at room temperature and at 70 °C, affording the corresponding formamide in 72% and 89% respectively (Table 4, entries 19–20).

A detailed comparison of *N*-formylation protocols from the literature is presented in the SI (Table 2), underscoring key differences in catalyst composition, loading, reaction conditions, reaction times, and yields. Conventional systems often rely on harsh thermal conditions, expensive nanostructured catalysts, organic solvents, or additional promoters to achieve acceptable performance, thereby limiting their practicality and scalability. In contrast, our protocol combines operational simplicity with sustainability: it employs a cost-effective catalyst design free of precious metals or complex supports, functions under relatively mild conditions, and delivers high selectivity at

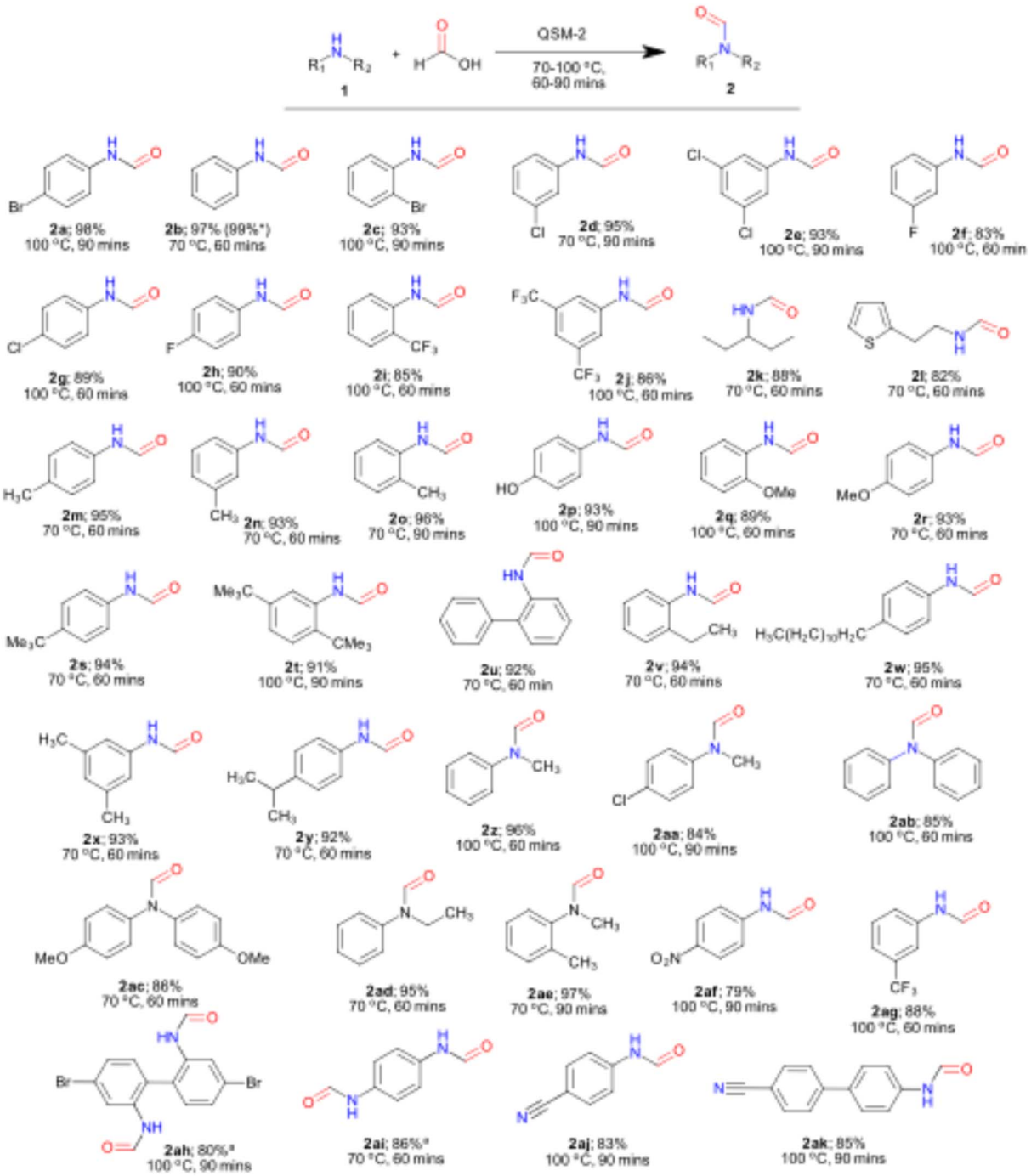

Fig. 7 *N*-formylation of amines using HCOOH in presence of QSM-2. [a]10 mmol formic acid was used.

low catalyst loading. Although the reaction time is comparable, this is offset by superior control over reactivity and cleaner product profiles, outperforming catalyst-free approaches that typically require prolonged heating and compromise selectivity. These attributes position our method as a robust and economically viable alternative for *N*-formylation chemistry.

With the optimised reaction conditions established, we proceeded to investigate the direct formylation of a wide range of amine substrates using formic acid, thereby assessing the versatility of the current methodology. A variety of primary and secondary amines were subjected to *N*-formylation with formic acid in the presence of QSM-2, resulting in the efficient formation of the corresponding formamides in good to excellent yields (79–98%) and with high selectivity (Fig. 7).

All substituted aromatic amines underwent clean and efficient *N*-formylation under the optimised conditions, yielding the desired products without the formation of side products. Anilines bearing weak electron-withdrawing groups resulted in

slightly lower yields (Fig. 7, entries **2f**, **2i**, **2j**, **2aa**, **2aj**, **2ak**). Aniline with a strong electron withdrawing group, such as $-NO_2$ substituent (**2af**), required a temperature of 100 °C and reaction time of 1.5 hours to yield the corresponding formamide. Similarly, other strongly electron withdrawing groups, such as –CN (**2aj**, **2ak**) and $-CF_3$ (**2i**, **2j**), also required elevated temperature (100 °C) to achieve good yields. 4-Chloroaniline was converted to the corresponding formamide in 1.5 hours at 70 °C, however, at 100 °C, the reaction was completed in 1 hour (Fig. 7, entry **2g**). Other halogenated aromatic amines, including **2c**, **2d**, **2e**, **2f**, **2h**, **2i**, and **2aa**, also demonstrated efficient *N*-formylation, reflecting the high performance of QSM-2. Aliphatic primary amines were also investigated under the optimised conditions and were found to undergo facile transformation to the corresponding formamides in good yields (Fig. 7, entries **2k** and **2l**). The scope was further extended to secondary amines, which afforded the corresponding formamides in excellent yields (Fig. 7, entries **2z**, **2aa**–**2ae**). Aromatic amines bearing sterically hindered substituents were well tolerated under the optimised conditions, undergoing efficient *N*-formylation without significant loss in yield (**2ab**, **2ac**, **2ad**). The *N*-formylation of aromatic diamines led to the formation of diformamides (**2ah**, **2ai**) in 85–86% yield. Overall, the methodology proved effective for the selective mono-formylation of primary amines, affording isolated yields in the range of 79–98%.

The structures of all synthesised formamides were confirmed by ^1H and ^{13}C NMR spectroscopy. Notably, ^1H NMR spectra of formamides indicated the presence of both *E* and *Z* isomers in solution. This observation is attributed to restricted rotation about the amide N–C(O) bond, which exhibits partial double-bond character due to resonance stabilisation. Consequently, these rotamers interconvert slowly on the NMR timescale due to the substantial rotational energy barrier associated with the amide linkage.[106]

These findings underscore the significant role and versatility of QSM-2 in the selective *N*-formylation of amines under mild, solvent-free conditions. The efficient conversion of both primary and secondary amines into their corresponding formamides highlights the efficacy of the high surface area mesoporous silica, offering an environmentally benign and broadly applicable strategy for sustainable formamide synthesis.

Conclusions

An efficient and scalable method for the synthesis of spherical silica with an ultra-high surface area (up to 1653 $m^2\ g^{-1}$) has been successfully developed under ambient conditions using CTAB as a structure-directing agent and β-cyclodextrin as an additive. Scale-up experiments confirmed the robustness and reproducibility of the protocol, enabling the preparation of 20 g batches without significant variation in physicochemical properties. Comprehensive characterisation, including X-ray diffraction, nitrogen physisorption, and FIB-TEM analyses, demonstrated the formation of highly porous materials with a narrow pore size distribution and a well-defined three-dimensional pore network, which accounts for the exceptional surface area observed in QSM-2. These findings underscore the potential of additive-assisted sol–gel strategies for tailoring porous materials with targeted textural properties.

This work establishes a robust and scalable strategy for the synthesis of ultra-high surface area silica (QSM-2) and demonstrates its utility as an efficient heterogeneous catalyst for sustainable chemical transformations. The material enabled selective *N*-formylation of a broad range of primary and secondary amines using formic acid as a renewable C_1 source, achieving good to excellent yields under mild, solvent-free conditions. The combination of exceptional textural properties and catalytic performance underscores the novelty of QSM-2 as a multifunctional platform for green chemistry. Importantly, the methodology is operationally simple, reproducible at gram-scale, and aligns with principles of atom economy and environmental sustainability.

Beyond *N*-formylation, the unique structural features of QSM-2 open avenues for its application in diverse chemical and biochemical processes, adsorption technologies, and energy-related systems. Future studies will focus on elucidating the mechanistic role of β-cyclodextrin in pore architecture development and exploring the integration of this additive-assisted sol–gel approach for designing next-generation porous materials with tuneable functionalities. Overall, this work provides a blueprint for bridging material design and sustainable catalysis, offering significant potential for industrial and environmental applications.

Author contributions

M. Anwar: conceptualisation, funding acquisition, methodology and scope development, investigation, supervision, data curation, analysis and interpretation, writing & editing of manuscript. S. Pathan: material synthesis & investigation, data curation, writing and reviewing of manuscript. S. P. Reddy: material synthesis & investigation, data curation, writing and reviewing of manuscript. (S. Pathan and S. P. Reddy have equal contribution). J. Ponraj: comprehensive TEM and FIB-TEM analysis. S. Dastgir: conceptualisation, funding acquisition, project administration, supervision, methodology and scope development, data analysis & interpretation, manuscript reviewing and editing.

Conflicts of interest

There are no conflicts to declare.

Data availability

The data supporting this study are available in the manuscript and its supplementary information (SI). Supplementary information: methods, experimental details, additional data, and NMR spectra. See DOI: https://doi.org/10.1039/d5ra07379k.

Acknowledgements

The authors acknowledge the financial support from Qatar National Research Fund (NPRP8-235-1-055, NPRP9-212-1-042,

and NPRP14S-0406-210154). HBKU Materials Core Labs' Staff; Dr S. Mansour, Dr M. A. Rana, Dr K. Mroue (SS NMR), M. Pasha (SEM), Dr A. R. Shetty (XRD) are greatly acknowledged for analytical support and helpful discussion.

References

1 C. T. Kresge, M. E. Leonowicz, W. J. Roth and J. C. Vartuli, *US Pat.*, 5098684A, 1992.
2 C. T. Kresge, M. E. Leonowicz, W. J. Roth and J. C. Vartuli, *US Pat.*, 5102643A, 1992.
3 C. T. Kresge, M. E. Leonowicz, W. J. Roth, J. C. Vartuli and J. S. Beck, *Nature*, 1992, **359**, 710–712.
4 J. S. Beck, J. C. Vartuli, W. J. Roth, M. E. Leonowicz, C. T. Kresge, K. D. Schmitt, C. T. W. Chu, D. H. Olson, E. W. Sheppard, S. B. McCullen, J. B. Higgins and J. L. Schlenker, *J. Am. Chem. Soc.*, 1992, **114**, 10834–10843.
5 D. Zhao, J. Feng, Q. Huo, N. Melosh, G. H. Fredrickson, B. F. Chmelka and G. D. Stucky, *Science*, 1998, **279**, 548–552.
6 S. Inagaki, Y. Fukushima and K. Kuroda, *J. Chem. Soc., Chem. Commun.*, 1993, 680–682.
7 S. Inagaki, A. Koiwai, N. Suzuki, Y. Fukushima and K. Kuroda, *Bull. Chem. Soc. Jpn.*, 1996, **69**, 1449–1457.
8 R. Ryoo, J. M. Kim, C. H. Ko and C. H. Shin, *J. Phys. Chem.*, 1996, **100**, 17718–17721.
9 S. A. Bagshaw, E. Prouzet and T. J. Pinnavaia, *Science*, 1995, **269**, 1242–1244.
10 Y. Li and J. Shi, *Adv. Mater.*, 2014, **26**, 3176–3205.
11 L. T. Gibson, *Chem. Soc. Rev.*, 2014, **43**, 5163–5172.
12 L. T. Gibson, *Chem. Soc. Rev.*, 2014, **43**, 5173–5182.
13 J. E. Lofgreen and G. A. Ozin, *Chem. Soc. Rev.*, 2014, **43**, 911–933.
14 X. Du and S. Z. Qiao, *Small*, 2015, **11**, 392–413.
15 C. Chen, J. Kim and W.-S. Ahn, *Korean J. Chem. Eng.*, 2014, **31**, 1919–1934.
16 C.-H. Lee, T.-S. Lin and C.-Y. Mou, *Nano Today*, 2009, **4**, 165–179.
17 S. Minakata and M. Komatsu, *Chem. Rev.*, 2009, **109**, 711–724.
18 A. Monnier, F. Schüth, Q. Huo, D. Kumar, D. Margolese, R. S. Maxwell, G. D. Stucky, M. Krishnamurty, P. Petroff, A. Firouzi, M. Janicke and B. F. Chmelka, *Science*, 1993, **261**, 1299–1303.
19 M. A. Karakassides, A. Bourlinos, D. Petridis, L. Coche-Guerènte and P. Labbè, *J. Mater. Chem.*, 2000, **10**, 403–408.
20 V. Alfredsson and M. W. Anderson, *Chem. Mater.*, 1996, **8**, 1141–1146.
21 H. Wang, W. Qian, J. Chen, Y. Wu, X. Xu, J. Wang and Y. Kong, *RSC Adv.*, 2014, **4**, 50832–50839.
22 T. Suteewong, H. Sai, R. Cohen, S. Wang, M. Bradbury, B. Baird, S. M. Gruner and U. Wiesner, *J. Am. Chem. Soc.*, 2011, **133**, 172–175.
23 S. Gómez, L. J. Garces, J. Villegas, R. Ghosh, O. Giraldo and S. L. Suib, *J. Catal.*, 2005, **233**, 60–67.
24 K. Schumacher, M. Grün and K. K. Unger, *Microporous Mesoporous Mater.*, 1999, **27**, 201–206.
25 J. Wang, J. Lu, J. Yang, W. Xiao and J. Wang, *Mater. Lett.*, 2012, **78**, 199–201.
26 C. Liu, S. Wang, Z. Rong, X. Wang, G. Gu and W. Sun, *J. Non-Cryst. Solids*, 2010, **356**, 1246–1251.
27 F. Gao, C. Lian, L. Zhou, H. Liu and J. Hu, *Langmuir*, 2014, **30**, 11284–11291.
28 M. Guo, Q. Liu, S. Lu, R. Han, K. Fu, C. Song, N. Ji, X. Lu, D. Ma and C. Liu, *Langmuir*, 2020, **36**, 11528–11537.
29 K. Hou, L. Shen, F. Li, Z. Bian and C. Huang, *J. Phys. Chem. B*, 2006, **110**, 9452–9460.
30 R. Ryoo, S. H. Joo and J. M. Kim, *J. Phys. Chem. B*, 1999, **103**, 7435–7440.
31 M. Kruk, M. Jaroniec, R. Ryoo and S. H. Joo, *Chem. Mater.*, 2000, **12**, 1414–1421.
32 K. Czechura and A. Sayari, *Chem. Mater.*, 2006, **18**, 4147–4150.
33 T.-W. Kim, P.-W. Chung and V. S. Y. Lin, *Chem. Mater.*, 2010, **22**, 5093–5104.
34 W. J. Kim, J. Churl Yoo and D. T. Hayhurst, *Microporous Mesoporous Mater.*, 2001, **49**, 125–137.
35 A. Okabe, T. Fukushima, K. Ariga, M. Niki and T. Aida, *J. Am. Chem. Soc.*, 2004, **126**, 9013–9016.
36 P. Schmidt-Winkel, P. Yang, D. I. Margolese, B. F. Chmelka and G. D. Stucky, *Adv. Mater.*, 1999, **11**, 303–307.
37 C. Yu, B. Tian, J. Fan, G. D. Stucky and D. Zhao, *J. Am. Chem. Soc.*, 2002, **124**, 4556–4557.
38 S. A. Bagshaw, *Chem. Commun.*, 1999, 1785–1786.
39 L. Wang, J. Zhang, F. Chen and M. Anpo, *J. Phys. Chem. C*, 2007, **111**, 13648–13651.
40 A. Sayari, *J. Am. Chem. Soc.*, 2000, **122**, 6504–6505.
41 R. Takahashi, S. Sato, T. Sodesawa, M. Kawakita and K. Ogura, *J. Phys. Chem. B*, 2000, **104**, 12184–12191.
42 Y. Yang, H. Yang, L. Liu, T. Li, H. Yuan and C. Ni, *J. Am. Ceram. Soc.*, 2017, **100**, 2502–2515.
43 H. I. Meléndez-Ortiz, Y. A. Perera-Mercado, L. A. García-Cerda, J. A. Mercado-Silva and G. Castruita, *Ceram. Int.*, 2014, **40**, 4155–4161.
44 P. Van Der Voort, M. Mathieu, F. Mees and E. F. Vansant, *J. Phys. Chem. B*, 1998, **102**, 8847–8851.
45 K. Schumacher, P. I. Ravikovitch, A. Du Chesne, A. V. Neimark and K. K. Unger, *Langmuir*, 2000, **16**, 4648–4654.
46 H. M. El-Zeiny, M. R. Abukhadra, O. M. Sayed, A. H. M. Osman and S. A. Ahmed, *Colloids Surf., A*, 2020, **586**, 124197.
47 S. Hong, Z. Li, C. Li, C. Dong and S. Shuang, *Appl. Surf. Sci.*, 2018, **427**, 1189–1198.
48 D. Horn and J. Rieger, *Angew. Chem., Int. Ed.*, 2001, **40**, 4330–4361.
49 F. Topuz and T. Uyar, *Beilstein J. Nanotechnol.*, 2018, **9**, 693–703.
50 A. Rimola, M. Fabbiani, M. Sodupe, P. Ugliengo and G. Martra, *ACS Catal.*, 2018, **8**, 4558–4568.
51 M. Nasrollahzadeh, N. Motahharifar, M. Sajjadi, A. M. Aghbolagh, M. Shokouhimehr and R. S. Varma, *Green Chem.*, 2019, **21**, 5144–5167.

52 A. Tlili, E. Blondiaux, X. Frogneux and T. Cantat, *Green Chem.*, 2015, **17**, 157–168.
53 T. Murata, M. Hiyoshi, M. Ratanasak, J.-y. Hasegawa and T. Ema, *Chem. Commun.*, 2020, **56**, 5783–5786.
54 E. Valeur and M. Bradley, *Chem. Soc. Rev.*, 2009, **38**, 606–631.
55 M. Anwar and M. G. Moloney, *Tetrahedron Lett.*, 2007, **48**, 7259–7262.
56 M. Anwar and M. G. Moloney, *Chem. Biol. Drug Des.*, 2013, **81**, 645–649.
57 T. Wada, H. Takagi, H. Minakami, W. Hamanaka, K. Okamoto, A. Ito and Y. Sahashi, *Science*, 1961, **134**, 195–196.
58 D. P. Tashkin, *Chronic Obstruct. Pulm. Dis.: Open Access.*, 2020, **15**, 3105–3122.
59 D. Lonsdale, *Med. Sci. Monit.*, 2004, **10**, Ra199–Ra203.
60 E. Ravina, *The Evolution of Drug Discovery: From Traditional Medicines to Modern Drugs*, Wiley-VCH, Weinheim, Germany, 2011.
61 J. Omprakash Rathi and G. Subray Shankarling, *ChemistrySelect*, 2020, **5**, 6861–6893.
62 C. L. Allen and J. M. J. Williams, *Chem. Soc. Rev.*, 2011, **40**, 3405–3415.
63 T. M. E. Dine, D. Evans, J. Rouden and J. Blanchet, *Chem.–Eur. J.*, 2016, **22**, 5894–5898.
64 L. Zhang, Z. Han, X. Zhao, Z. Wang and K. Ding, *Angew. Chem., Int. Ed.*, 2015, **54**, 6186–6189.
65 F. F. Blicke and C.-J. Lu, *J. Am. Chem. Soc.*, 1952, **74**, 3933–3934.
66 P. Ganapati Reddy, G. D. Kishore Kumar and S. Baskaran, *Tetrahedron Lett.*, 2000, **41**, 9149–9151.
67 C. J. Gerack and L. McElwee-White, *Molecules*, 2014, **19**, 7689–7713.
68 P. Strazzolini, A. G. Giumanini and S. Cauci, *Tetrahedron*, 1990, **46**, 1081–1118.
69 R. E. Patre, S. Mal, P. R. Nilkanth, S. K. Ghorai, S. H. Deshpande, M. El Qacemi, T. Smejkal, S. Pal and B. N. Manjunath, *Chem. Commun.*, 2017, **53**, 2382–2385.
70 M. Sakurai, R. Kawakami and N. Kihara, *Tetrahedron Lett.*, 2019, **60**, 1291–1294.
71 R. S. L. Chapman, R. Lawrence, J. M. J. Williams and S. D. Bull, *Org. Lett.*, 2017, **19**, 4908–4911.
72 N. Ortega, C. Richter and F. Glorius, *Org. Lett.*, 2013, **15**, 1776–1779.
73 H. Yu, Z. Wu, Z. Wei, Y. Zhai, S. Ru, Q. Zhao, J. Wang, S. Han and Y. Wei, *Commun. Chem.*, 2019, **2**, 15.
74 P. Daw, S. Chakraborty, G. Leitus, Y. Diskin-Posner, Y. Ben-David and D. Milstein, *ACS Catal.*, 2017, **7**, 2500–2504.
75 Z. Wu, Y. Zhai, W. Zhao, Z. Wei, H. Yu, S. Han and Y. Wei, *Green Chem.*, 2020, **22**, 737–741.
76 X. Wu, Y. Chen, B. Tang, Q. Yan, D. Wu, H. Zhou, H. Wang, H. Zhang, D. He, H. Li, J. Zeng, L. Lu, S. Yang and T. Ma, *Nat. Commun.*, 2025, **16**, 8785.
77 V. B. Saptal, T. Sasaki and B. M. Bhanage, *ChemCatChem*, 2018, **10**, 2593–2600.
78 J. Fang, Z.-Q. Wang, X. Wei, Y. Ma, H. Gong, X.-Q. Gong and Z. Hou, *ACS Sustainable Chem. Eng.*, 2021, **9**, 13256–13267.
79 Y. Zhang, J. Wang, H. Zhu and T. Tu, *Chem.–Asian J.*, 2018, **13**, 3018–3021.
80 C. Federsel, A. Boddien, R. Jackstell, R. Jennerjahn, P. J. Dyson, R. Scopelliti, G. Laurenczy and M. Beller, *Angew. Chem., Int. Ed.*, 2010, **49**, 9777–9780.
81 X. Luo, H. Zhang, Z. Ke, C. Wu, S. Guo, Y. Wu, B. Yu and Z. Liu, *Sci. China Chem.*, 2018, **161**, 725–731.
82 R. Luo, X. Lin, Y. Chen, W. Zhang, X. Zhou and H. Ji, *ChemSusChem*, 2017, **10**, 1224–1232.
83 C. Xie, J. Song, H. Wu, B. Zhou, C. Wu and B. Han, *ACS Sustainable Chem. Eng.*, 2017, **5**, 7086–7092.
84 C. Das Neves Gomes, O. Jacquet, C. Villiers, P. Thuéry, M. Ephritikhine and T. Cantat, *Angew. Chem., Int. Ed.*, 2012, **51**, 187–190.
85 J. Hou, J.-H. Xie and Q.-L. Zhou, *Angew. Chem., Int. Ed.*, 2015, **54**, 6302–6305.
86 J. Hou, M.-L. Yuan, J.-H. Xie and Q.-L. Zhou, *Green Chem.*, 2016, **18**, 2981–2984.
87 M.-C. Fu, R. Shang, W.-M. Cheng and Y. Fu, *ACS Catal.*, 2016, **6**, 2501–2505.
88 Y. Wang, Y. Zeng, B. Yang and Y. Shi, *Org. Chem. Front.*, 2016, **3**, 1131–1136.
89 Y.-N. Li, L.-N. He, X.-D. Lang, X.-F. Liu and S. Zhang, *RSC Adv.*, 2014, **4**, 49995–50002.
90 M. He, Y. Sun and B. Han, *Angew. Chem., Int. Ed.*, 2013, **52**, 9620–9633.
91 S. Kazemi, A. Mobinikhaledi and M. Zendehdel, *Chin. Chem. Lett.*, 2017, **28**, 1767–1772.
92 X. Chen, Y. Liu and J. Wu, *Mol. Catal.*, 2020, **483**, 110716.
93 D. Wei, R. Sang, P. Sponholz, H. Junge and M. Beller, *Nat. Energy*, 2022, **7**, 438–447.
94 A. Rosas-Hernández, H. Junge and M. Beller, *ChemCatChem*, 2015, **7**, 3316–3321.
95 L. Yu, Q. Zhang, S.-S. Li, J. Huang, Y.-M. Liu, H.-Y. He and Y. Cao, *ChemSusChem*, 2015, **8**, 3029–3035.
96 R. B. Nasir Baig, S. Verma, M. N. Nadagouda and R. S. Varma, *Green Chem.*, 2016, **18**, 1019–1022.
97 V. Thakur, A. Kumar, N. Sharma, A. K. Shil and P. Das, *Adv. Synth. Catal.*, 2018, **360**, 432–437.
98 M. Li, L. Hu, X. Cao, H. Hong, J. Lu and H. Gu, *Chem.–Eur. J.*, 2011, **17**, 2763–2768.
99 Y. Wei, J. Wu, D. Xue, C. Wang, Z. Liu, Z. Zhang, G. Chen and J. Xiao, *Synlett*, 2014, **25**, 1295–1298.
100 H. Liang, T. Zhao, J. Ou, J. Liu and X. Hu, *ACS Sustainable Chem. Eng.*, 2023, **11**, 14317–14322.
101 J. H. Shin and M. H. Schoenfisch, *Chem. Mater.*, 2008, **20**, 239–249.
102 L. T. Zhuravlev, *Colloids Surf., A*, 2000, **173**, 1–38.
103 E. L. Fought, Y. Han, T. L. Windus, I. I. Slowing, T. Kobayashi and J. W. Evans, *Microporous Mesoporous Mater.*, 2022, **341**, 112077.
104 K. S. W. Sing, *Pure Appl. Chem.*, 1982, **54**, 2201–2218.
105 J. Xu, Z. Luan, H. He, W. Zhou and L. Kevan, *Chem. Mater.*, 1998, **10**, 3690–3698.
106 Q. Zhang, X.-T. Lin, N. Fukaya, T. Fujitani, K. Sato and J.-C. Choi, *Green Chem.*, 2020, **22**, 8414–8422.